ADVANCED MATERIALS
www.advmat.de

Design of Fluorinated Elastomeric Electrolyte for Solid-State Lithium Metal Batteries Operating at Low Temperature and High Voltage

*Jinseok Park, Hyeonseok Seong, Chanho Yuk, Dongkyu Lee, Youyoung Byun, Eunji Lee, Wonho Lee, and Bumjoon J. Kim**

This work demonstrates the low-temperature operation of solid-state lithium metal batteries (LMBs) through the development of a fluorinated and plastic-crystal-embedded elastomeric electrolyte (F-PCEE). The F-PCEE is formed via polymerization-induced phase separation between the polymer matrix and plastic crystal phase, offering a high mechanical strain (≈300%) and ionic conductivity (≈0.23 mS cm^{-1}) at −10 °C. Notably, strong phase separation between two phases leads to the selective distribution of lithium (Li) salts within the plastic crystal phase, enabling superior elasticity and high ionic conductivity at low temperatures. The F-PCEE in a Li/LiNi$_{0.8}$Co$_{0.1}$Mn$_{0.1}$O$_2$ full cell maintains 74.4% and 42.5% of discharge capacity at −10 °C and −20 °C, respectively, compared to that at 25 °C. Furthermore, the full cell exhibits 85.3% capacity retention after 150 cycles at −10 °C and a high cut-off voltage of 4.5 V, representing one of the highest cycling performances among the reported solid polymer electrolytes for low-temperature LMBs. This work attributes the prolonged cycling lifetime of F-PCEE at −10 °C to the great mechanical robustness to suppress the Li-dendrite growth and ability to form superior LiF-rich interphases. This study establishes the design strategies of elastomeric electrolytes for developing solid-state LMBs operating at low temperatures and high voltages.

1. Introduction

Lithium (Li) metal batteries (LMBs) are pivotal in advancing next-generation battery technology, owing to the high theoretical capacity (3860 mAh g^{-1}) and low electrochemical potential (−3.04 V versus the standard hydrogen electrode) of Li metal.[1–3] Despite significant efforts to develop high-energy and long-cycling LMBs, achieving sufficient performance under extreme conditions for advanced applications remains a challenge.[4–6] These applications encompass mobility and other technologies operating in subzero conditions, including high-altitude and polar regions of the Earth, deep-sea environments, or outer space.[7–9] However, the use of existing organic liquid electrolytes in LMBs often leads to reduced battery lifetime and safety issues. These issues are primarily associated with the formation of Li-dendrite and unstable solid-electrolyte-interphase (SEI), which can be exacerbated by slow Li^+ transport and charge transfer kinetics at low temperatures.[7,10] Solid-state electrolytes (SSEs) are a promising strategy, potentially offering higher energy density and improved safety over conventional liquid electrolytes.[11–13] Nevertheless, the SSE-based LMBs operating at low temperatures are scarcely explored, primarily due to the low ionic conductivity of SSEs and large interfacial resistance between SSE and electrodes at low temperatures.[8,9]

Solid polymer electrolytes (SPEs) have attracted great interest due to their inherent advantages such as high flexibility, lightweight, and easy processability, which distinguish them from inorganic SSEs.[14–16] In particular, SPEs can be utilized through the in situ polymerization method to form a conformal contact at the electrode/electrolyte interface, effectively reducing interfacial resistance.[16,17] However, SPEs have suffered from low ionic conductivity and lack of mechanical integrity to suppress Li dendrite growth, thereby limiting the electrochemical performances of SPE-based LMBs at low temperatures.[7,18,19] To overcome these limitations, various design strategies have been proposed to improve the low-temperature performances of SPE-based LMBs. For example, incorporating a plasticizer into the polymer matrix enhances the segmental motion of

J. Park, H. Seong, D. Lee, B. J. Kim
Department of Chemical and Biomolecular Engineering
Korea Advanced Institute of Science and Technology (KAIST)
Daejeon 34141, Republic of Korea
E-mail: bumjoonkim@kaist.ac.kr
C. Yuk, W. Lee
Department of Polymer Science and Engineering
Department of Energy Engineering Convergence
Kumoh National Institute of Technology
Gumi, Gyeongbuk 39177, Republic of Korea
Y. Byun, E. Lee
School of Materials Science and Engineering
Gwangju Institute of Science and Technology (GIST)
Gwangju 61005, Republic of Korea

The ORCID identification number(s) for the author(s) of this article can be found under https://doi.org/10.1002/adma.202403191

DOI: 10.1002/adma.202403191

polymer chains, thereby increasing Li^+ conductivity at low temperatures.[20–24] Also, the incorporation of inorganic fillers in a polymer/ceramic composite electrolyte can effectively enhance mechanical robustness and suppress Li dendrite growth.[25–27] Alternatively, employing soft SPEs with rubbery or viscoelastic characteristics can uniformly cover the Li metal surface and effectively accommodate volume changes of Li metal anode during battery cycling, thus mitigating Li dendrite growth.[28,29] Despite these advancements, developing SPEs for stable operation in LMBs at subzero temperatures remains a significant, and ongoing challenge.

Insights from the previous studies suggest that SPEs should satisfy the following requirements for operating LMBs at low temperatures: (1) High ionic conductivity at low temperatures, ideally through a three-dimensional ion-conducting pathway. (2) High retention of soft characteristics with high mechanical flexibility and resilience. This is vital to accommodate significant volume changes in Li and to suppress Li dendrite growth.[19] Additionally, strong adhesion between the SPEs and electrodes is crucial to prevent contact loss from the large volume changes during cycling.[27,30] (3) A chemical structure of SPE that promotes the formation of a favorable LiF-rich SEI layer, which is critical for achieving high cycling stability of LMBs.[31,32] This aspect becomes particularly important as kinetically sluggish Li^+ transport and charge transfer at a low temperature can accelerate the formation of unfavorable SEI layers and Li dendrite.[32–34] Polymerization-induced phase separation (PIPS) method has the potential to fabricate SPEs meeting these requirements by creating a bicontinuous structure consisting of an ion-conducting phase and polymer matrix.[35,36] Despite the typical trade-off relationship between high mechanical robustness and ionic conductivity in polymeric materials, the bicontinuous structure allows for the independent optimization of each phase and facilitates the development of SPEs with both superior ionic conductivity and mechanical properties. For example, plastic crystal-embedded elastomeric electrolyte (PCEE) developed via PIPS exhibits high ionic conductivity through the plastic crystal phase and high mechanical robustness of the elastomeric phase, enabling high-performance LMBs at room temperature.[37,38] Therefore, we envision that the fabrication of PCEE-based SPEs fulfilling the above criteria could facilitate the high cycling performance of LMBs at subzero temperatures.

In this study, we develop a fluorine (F)-containing, plastic-crystal-embedded elastomeric electrolyte (F-PCEE) to achieve stable operation of solid-state LMBs at −10 °C. The F-PCEE features a bicontinuous structure, consisting of a succinonitrile (SN) based plastic crystal phase embedded within a 2,2,3,4,4,4-hexafluorobutyl acrylate (HFBA) based elastomer matrix. Importantly, the F-PCEE exhibits high Li ion conductivity (0.23 mS cm^{-1}) at −10 °C and enhanced elastic properties with ≈300% strain at fracture, overcoming the trade-off between ion conducting and mechanical properties. The confinement of dominant Li^+ content in the plastic crystal phase of F-PCEE is a key factor in obtaining both high ionic conductivity and exceptional mechanical elasticity at low temperatures. Furthermore, the use of the fluorine-containing F-PCEE facilitates the formation of the LiF-rich SEI layer, enabling the stable cycling of the LMBs at −10 °C. The Li||F-PCEE||Li symmetric cell demonstrates notable cycling stability, showing more than 1500 h of operation at −10 °C. In addition, the F-PCEE in a full cell with the Li metal anode and the $LiNi_{0.8}Co_{0.1}Mn_{0.1}O_2$ (NCM811) cathode at −10 °C exhibits excellent performance with 85.3% capacity retention after 150 cycles at 0.1 C and a high cut-off voltage of 4.5 V. This is one of the highest cycling performances of SPE-based LMBs operating at −10 °C, particularly with the Ni-rich cathode system. In contrast, the reference poly(butyl acrylate)-based PCEE (BA-PCEE) shows lower ionic conductivity and inferior mechanical properties at −10 °C, resulting in the rapid capacity decay in the full cell. Therefore, this study highlights the design strategies of elastomeric electrolytes for constructing low-temperature operating solid-state LMBs.

2. Results and Discussion

The superior ionic conductivity, mechanical resilience, and the ability to form a stable SEI layer of the SPEs at low temperatures are important prerequisites for fabricating solid-state LMBs that can effectively operate at low temperatures. To fulfill these requirements, we designed a bicontinuous structured F-PCEE comprising a fluorine-containing elastomer and SN plastic crystal phases, serving as the mechanical scaffold and ion-conducting domain, respectively (**Scheme 1**). This bicontinuous structure enables the independent optimization of each phase to yield the F-PCEE with high mechanical properties and ionic conductivity at low temperatures while the F-chemistry enhances the cycling stability of LMBs. Based on this design strategy, the F-PCEE possesses the following advantages. (1) The chemical incompatibility between the hydrophobic HFBA and hydrophilic SN leads to Li salts being predominantly localized within the continuous SN phase through PIPS. This configuration significantly enhances the Li^+ conductivity of the F-PCEE. (2) Conversely, the low Li-salt concentration within the polymer matrix allows for the construction of an elastomer matrix with a low glass transition temperature (T_g), which is crucial for maintaining the superior mechanical resilience of the elastomer matrix at low temperatures. (3) The F-chemistry inherent to the F-PCEE enhances its oxidative stability and facilitates the formation of LiF-rich SEI layers, offering good interfacial stability for solid-state LMBs operating at low temperatures. We anticipate that the combined benefits of the F-PCEE will enable superior cycling performance of LMBs under challenging conditions such as a low temperature and wide voltage window.

The F-PCEE was synthesized through a thermally activated polymerization and cross-linking process of a precursor solution consisting of HFBA, SN, poly(ethylene glycol) diacrylate (PEGDA, cross-linker), azobisisobutyronitrile (AIBN, thermal initiator), lithium bis(trifluoromethanesulfonyl)imide (LiTFSI), and lithium difluoro(oxalato)borate (LiDFOB). The detailed synthetic procedure is described in Experimental Section. Tuning the morphology of the polymer and plastic crystal phases is critical for achieving the mechanical robustness of the F-PCEE while preserving high Li-ion conductivity.[38,39] For the optimization of the physicochemical properties of F-PCEE, we varied the volume fraction of SN (f_{SN}) between 0.4 and 0.6. In F-PCEE, we applied a dual salt system consisting of LiTFSI and LiDFOB with a fixed molar ratio of 8:2, because the use of LiDFOB can effectively suppress the corrosion of the aluminum (Al) current collector during repeated cycling.[40,41] Due to the limited solubility of LiDFOB

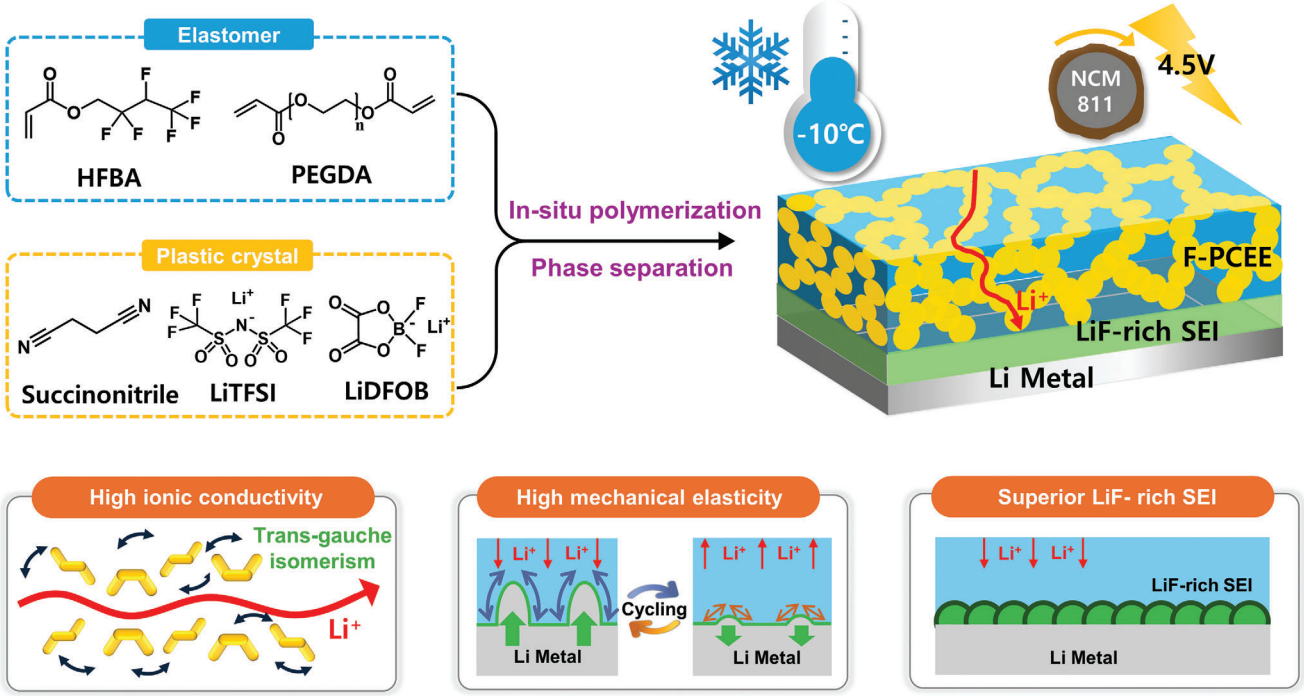

Scheme 1. The design of fluorinated elastomeric electrolytes with components in the elastomer and plastic crystal phases. The poly(HFBA) matrix exhibits mechanical elasticity and the ability to form LiF-rich solid-electrolyte-interphase (SEI) layers, while the solid plastic crystal phase efficiently transports Li^+ via trans-gauch isomerism at a low temperature.

in the F-PCEE precursor solution, the 0.8 M LiTFSI and 0.2 M LiDFOB were used to maintain high ionic conductivity and effectively protect the Al current collector. All the F-PCEEs with f_{SN} between 0.4 and 0.6 show solid and opaque appearances (**Figure 1a**), suggesting the development of a phase-separated structure between the cross-linked poly(HFBA) matrix and the SN phase.

The distribution of Li^+ in F-PCEE at different f_{SN} values was investigated using ^7Li solid-state nuclear magnetic resonance (NMR) spectroscopy (Figure 1b). The ^7Li NMR spectra of F-PCEE reveal two distinct peaks at −1.49 and −2.25 ppm, corresponding to Li^+ interactions with the cross-linked poly(HFBA) matrix and SN, respectively. This indicates the presence of distinct poly(HFBA) and plastic crystal phases within F-PCEE. In addition, the deconvoluted ^7Li NMR spectra indicate that the majority of Li^+ exists within the SN phase, owing to their greater affinity for the hydrophilic SN compared to the hydrophobic HFBA (Figure S1, Supporting Information). Consequently, the Li^+ concentration in the SN phase increases with higher f_{SN}. Specifically, the areal ratio of the Li^+ peak in poly(HFBA) and SN phases increases from 2.6 to 4.6 as the f_{SN} increases from 0.40 to 0.60. The coordination between the Li^+ and PEGDA was not distinctly identified in the NMR spectra, possibly due to the weak intensity from the minor quantity of PEGDA and the dominant interaction of Li^+ with the SN phase. The ionic conductivity (σ) and tortuosity (τ) of F-PCEE at 25 °C were evaluated as a function of f_{SN} (Figure 1c). The σ values gradually increase with increasing f_{SN}, and the F-PCEE with $f_{SN} \geq 0.50$ exhibits fast ion transport with σ values exceeding 1.1 mS cm^{-1}. The increase in σ with the higher f_{SN} can be attributed to the larger fraction of the ion-conducting SN phase. Furthermore, the increase in the f_{SN} leads to the gradual decrease in τ from 2.1 for $f_{SN} = 0.40$ to 1.6 for $f_{SN} = 0.60$. Notably, the τ values of the F-PCEEs at $0.4 < f_{SN} < 0.6$ suggest efficient ion transport in the F-PCEEs through 3D interconnected pathways, as it is reported that an ideal bicontinuous network exhibits the τ value between 1.5 and 3.0.[38,42] The importance of tuning f_{SN} value has been demonstrated in our previous study, as a certain amount of SN is required for developing bicontinuous structures with percolated SN channels.[38] At $f_{SN} < 0.4$, the ionic conductivity of F-PCEE sharply decreases to 0.81 mS cm^{-1}, 0.14 mS cm^{-1}, and 3.2×10^{-4} mS cm^{-1} at f_{SN} of 0.4, 0.3, and 0.1, respectively, due to the lack of percolated SN channels with decreasing f_{SN} (Figure S2, Supporting Information).

The mechanical elasticity and robustness of SPEs are critical to withstand the repeated volume changes of electrodes during cycling, suppress Li dendrite growth, and endure external impacts during use.[19,28,29] In this regard, we evaluated the mechanical elasticity of F-PCEE by obtaining the stress-strain curves using a universal testing machine (UTM) (Figure 1d). F-PCEE samples at $0.40 < f_{SN} < 0.60$ exhibit typical elastomeric behavior as shown by the strain values at fracture exceeding 150%. Notably, the F-PCEE with $f_{SN} = 0.54$ displays the highest strain value of ≈250% at fracture. However, when f_{SN} increases to 0.60, both ultimate stress and strain at fracture decrease due to the reduced volume fraction of the elastomeric poly(HFBA) matrix. The F-PCEE with a higher f_{SN} of 0.70 loses most of its elastomeric properties because the minor elastomer phase fails to surround the fragile SN phase and is unable to dissipate the mechanical stress during stretching/releasing. Therefore, we determine that the F-PCEE formulated at $f_{SN} = 0.54$ represents the optimal F-PCEE SPE with balanced ionic conductivity and mechanical

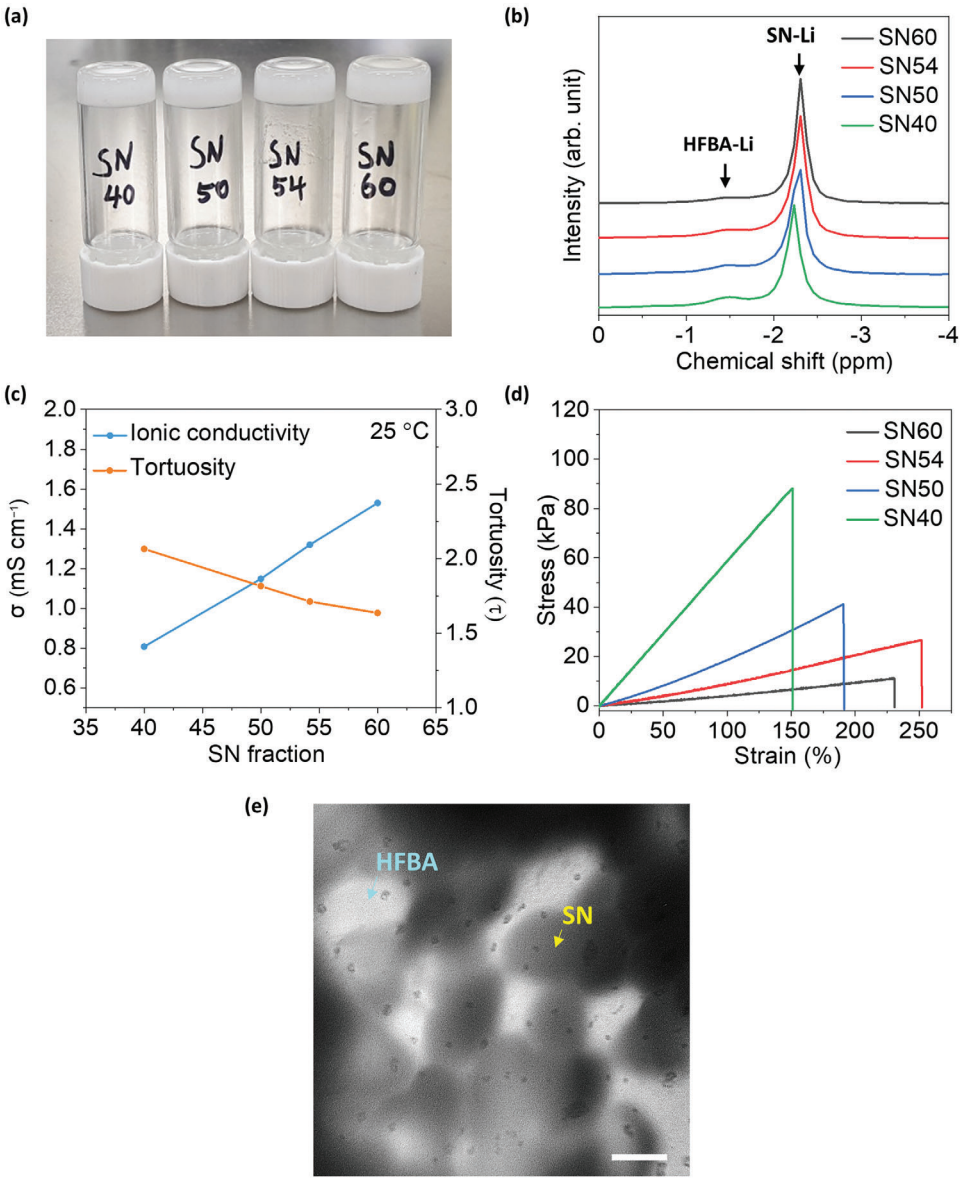

Figure 1. a) The photo image, b) ^{7}Li solid-state NMR spectra, c) ionic conductivity (σ) with corresponding tortuosity (τ), and d) stress–strain curve of F-PCEE with varying ratios of SN and HFBA at 25 °C. e) Cryo-TEM image of F-PCEE. The scale bar is 500 nm.

properties for further investigation in the LMBs. Upon fabricating F-PCEE at f_{SN} = 0.54, Fourier-transform infrared spectroscopy (FTIR) confirmed the full conversion of HFBA monomers and PEGDA cross-linkers into the elastomer matrix (Figure S3, Supporting Information). Additionally, thermogravimetric analysis (TGA) demonstrated good thermal stability with the onset of degradation at ≈150 °C (Figure S4, Supporting Information). The cryogenic transmission electron microscopy (cryo-TEM) was utilized to characterize the cross-sectional morphology of F-PCEE, confirming the phase separated structure between the HFBA and SN domains on the length scale of a few hundred nanometers (Figure 1e).

To elucidate the impact of the chemical structure of F-PCEE on the mechanical and electrochemical properties, we synthesized a reference sample of BA-PCEE featuring a bicontinuous structure of poly(BA) matrix and SN phase. The synthetic procedure of the BA-PCEE is described in Experimental Section and previous literature.[39] The primary distinction lies in the chemical structures of the elastomer matrix of BA-PCEE, which consists of BA monomers without F atoms while retaining the SN phase (f_{SN} = 0.50) with LiTFSI and LiDFOB salts. The BA-PCEE showed high discharge capacity and good cycling performance in LMBs at room temperature, but the discharge capacity rapidly decreased at 0 °C.[37] For the comparative analysis, we evaluated the temperature-dependent mechanical properties of F-PCEE and BA-PCEE over a wide temperature range of −30–25 °C using UTM. The F-PCEE demonstrates remarkable elastomeric behavior at low temperatures, exhibiting high strain at fracture (≈300%) at both −10 °C and −20 °C (**Figure 2a**). The increase in strain at fracture values at −10 °C

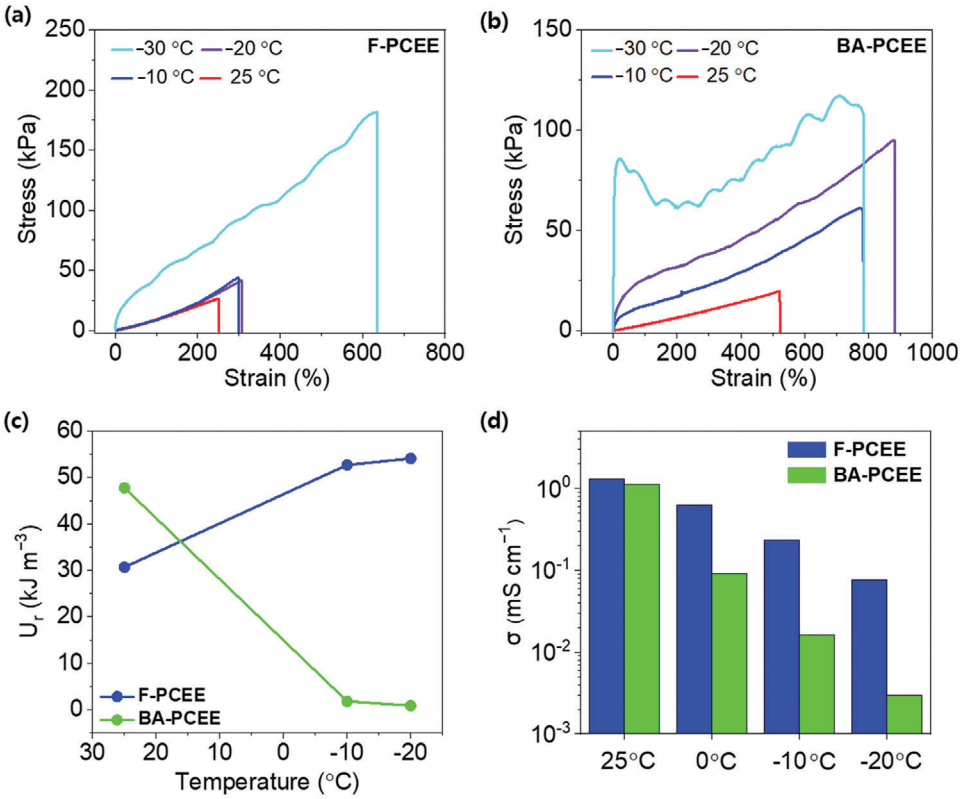

Figure 2. Stress–strain curves of a) F-PCEE and b) BA-PCEE at 25 °C, −10 °C, −20 °C, and −30 °C. c) Modulus of resilience (U_r) of F-PCEE and BA-PCEE calculated from the elastic region of the stress–strain curves. d) Ionic conductivity (σ) of F-PCEE and BA-PCEE at 25 °C, 0 °C, −10 °C, and −20 °C.

and −20 °C compared to that at 25 °C indicates the enhanced elasticity of the F-PCEE under reduced temperatures, which is attributed to the entropy-driven elasticity of elastomers for compensating the exothermic process during stretching.[43–45] However, as the temperature approaches the T_g of the polymeric matrix, the elastomers lose their elastic property and show a plastic behavior. Therefore, the elastomeric behavior of F-PCEE at −20 °C aligns well with its low T_g of −47 °C as determined by differential scanning calorimetry (DSC) (Figure S5, Supporting Information). In contrast, the BA-PCEE, which exhibits elastomeric behavior at 25 °C, shows irreversible plastic deformation below −10 °C (Figure 2b). To clearly show the elastic limit of the BA-PCEE at low temperatures, the initial parts of stress–strain curves of F-PCEE and BA-PCEE at −20 °C, −10 °C, and 25 °C are provided in Figure S6 (Supporting Information). Also, the cyclic stress–strain curves at −10 °C confirm the superior mechanical elasticity of F-PCEE compared to the BA-PCEE (Figure S7, Supporting Information). The discrepancy in the mechanical properties between the F-PCEE and BA-PCEE becomes markedly pronounced at −30 °C. At this temperature, the BA-PCEE entirely loses its elastic property and displays a distinct necking behavior due to its T_g of −20 °C.[37]

The inelastic behavior of SPEs can compromise the interfacial contact and degrade the dimensional stability of the battery cells over time, adversely affecting battery performance.[46,47] While toughness can be an important mechanical property for preventing the fracture of solid electrolytes, the transition from rubbery elastomer to a glassy state can also lead to an increase in toughness.[48] As shown in Figure S8 (Supporting Information), the toughness of F-PCEE and BA-PCEE noticeably increases at −30 °C and −10 °C, respectively, corresponding to their transition from elastic to plastic deformation. At these temperatures, the glassy polymers show irreversible deformation under small strain due to the significantly decreased elastic limit. Therefore, we quantitatively evaluated the elasticity of both F-PCEE and BA-PCEE by calculating the modulus of resilience (U_r) (Figure 2c), which represents the maximum energy that can be reversibly stored within the elastic region of the materials. Thus, the U_r values correspond to the area of the elastic region in the stress-strain curve. Both F-PCEE and BA-PCEE exhibit remarkably high U_r values of over 30.0 kJ m^{-3} at 25 °C, which is more than 10-fold the U_r value of poly(ethylene oxide)-based SPE with 40 wt% LiTFSI (U_r = 3.0 kJ m^{-3}).[47] At lower temperatures of −10 °C and −20 °C, the U_r values for F-PCEE increase to 52.7 and 54.1 kJ m^{-3}, respectively, indicating highly resilient mechanical properties of F-PCEE at low temperatures. We note that these U_r values are comparably high to that (U_r = 67.0 kJ m^{-3}) of the commercial Celgard 3501 separator used in the conventional liquid electrolyte system.[49] In contrast, the U_r value of BA-PCEE significantly decreases from 47.8 to 0.9 kJ m^{-3} when the temperature decreases from 25 °C to −10 °C, highlighting the superior mechanical resilience of F-PCEE at low temperatures compared to BA-PCEE. Additionally, it is noteworthy that gel electrolytes embedding large amounts of solvent generally show poor mechanical properties with inelastic deformation and fracture at small strains, whereas the F-PCEE with bicontinuous structure shows

high mechanical elasticity.[47,50] Overall, the mechanical properties of the F-PCEE demonstrate its great potential for accommodating large Li volume change and suppressing Li dendrite during cycling at low temperatures.

The distinct mechanical elasticity and resilience of F-PCEE at the low temperature of −20 °C aligns well with the lower T_g (−47 °C) of the poly(HFBA) matrix compared to the T_g (−20 °C) of the poly(BA) matrix of BA-PCEE. In general, the increase of ion concentration in polymer electrolytes increases the T_g of the materials, due to the formation of quasi-ionic cross-links between the ion species and polymer chains.[51–55] Therefore, the low T_g of F-PCEE is mainly attributed to the poly(HFBA) matrix with low Li content, driven by the strong phase separation between the poly(HFBA) and SN phases, as well as the preferential localization of Li within the SN phase (Figure S1, Supporting Information). In comparison, the nonfluorinated poly(BA) matrix exhibits a stronger preference for Li ions compared to the poly(HFBA) matrix, resulting in the comparable amount of Li within the poly(BA) and SN phases in BA-PCEE as identified by ^{7}Li NMR spectra (Figure S9, Supporting Information).

The tuning of the phase-separated structure and T_g of the polymer matrix further explain the importance of the F-PCEE design to obtain high ionic conductivity at low temperatures (Figure 2d). While the F-PCEE shows higher σ compared to the BA-PCEE across all the temperatures ranging from −20 °C to 25 °C, the difference in the σ values between the two systems becomes more pronounced at lower temperatures. At 25 °C, the σ values for the F-PCEE and BA-PCEE were 1.32 and 1.13 mS cm^{-1}, respectively. However, at −10 °C, the F-PCEE exhibits a significantly higher σ of 0.23 mS cm^{-1} compared to the BA-PCEE (σ = 0.016 mS cm^{-1}). Furthermore, at −20 °C, the F-PCEE shows a 25-fold greater σ value (0.077 mS cm^{-1}) compared to the BA-PCEE (σ = 0.003 mS cm^{-1}) (Figure 2d). The following factors contribute to the significant discrepancy in σ values between the F-PCEE and BA-PCEE at lower temperatures. First, the higher σ of F-PCEE can be attributed to a higher Li^+ concentration within the SN domains of F-PCEE compared to BA-PCEE, as indicated by the ^{7}Li NMR (Figure 1b and Figure S9, Supporting Information). In addition, due to the extremely slow segmental motion of the poly(BA) matrix near T_g, the contribution of the Li^+ conductivity within the poly(BA) matrix can be negligible at temperatures below −10 °C.[56]

Next, the electrochemical performance of BA-PCEE and F-PCEE at 25 °C was investigated by using a full cell configured with a 40-µm-thick Li anode and a $LiNi_{0.8}Co_{0.1}Mn_{0.1}O_2$ (NCM811) cathode. The detailed electrochemical characteristics of BA-PCEE at 25 °C have been studied in our previous reports and the cycling performance in a full cell is provided in Figure S10 (Supporting Information).[37–39] The BA-PCEE showed high cycling performance in LMBs in the voltage range of 2.7–4.5 V at 25 °C. For comparison, the F-PCEE was in situ polymerized between the electrodes to ensure great adhesion properties and low interfacial resistance. The in situ polymerized F-PCEE indicates a much stronger adhesion energy of 18.4 J m^{-2} compared to the 8.0 J m^{-2} of ex situ polymerized F-PCEE (Figure S11, Supporting Information). The strong adhesion between the elastomeric electrolyte and electrodes is important to accommodate the substantial volume change and mitigate Li dendrite growth during cycling.[30,37,57] The electrochemical floating test of F-PCEE was conducted to investigate the electrochemical window (**Figure 3a**). The excellent oxidation stability of F-PCEE was confirmed by the low leakage current (<2 µA) at a high voltage of 4.5 V, indicating the stable operation of Li||F-PCEE||NCM811 full cells up to 4.5 V. The oxidation stability of F-PCEE was further validated through the anodic linear-sweep voltammetry (LSV), which indicated an onset of oxidation at ≈4.75 V (Figure S12, Supporting Information). The superior oxidative stability of the F-PCEE is attributed to the high bond energy of F chemistry (e.g., C−F).[58] Thus, we conducted the cycling stability test at a wide cutoff voltage window of 2.7–4.5 V. The F-PCEE full cell exhibits 85.7% capacity retention (157 mAh g^{-1}) with an average Coulombic efficiency (CE) of 99.5% after 150 cycles at 0.5 C (Figures 3b,c). We further confirmed the great cycling performance of F-PCEE in replicated full cells (Figure S13, Supporting Information).

Based on the excellent electrochemical performances of F-PCEE at room temperature, we explored its application in low-temperature operating LMBs. Notably, the F-PCEE at −10 °C exhibits highly adhesive properties with an adhesion energy of 43.3 J m^{-2}, surpassing twice the observed value at room temperature (Figure S14, Supporting Information). The enhanced adhesion force can be attributed to the decreased molecular mobility of F-PCEE at low temperatures.[59] Combined with the great mechanical resilience and adhesive property of F-PCEE at −10 °C, the F-PCEE can effectively accommodate large volume change without delamination at interfaces and prevent Li dendrite growth during charge/discharge cycling at a low temperature. Then, we conducted the Li plating and stripping test at −10 °C in a symmetric Li cell by gradually increasing current density from 0.1 to 0.2, 0.5, and 1.0 mA cm^{-2} and maintaining at 1.0 mA cm^{-2} (1.0 mAh cm^{-2}) (Figure S15, Supporting Information). The polarization proportionally increases from 28 mV at 0.1 mA cm^{-2} to 280 mV at 1.0 mA cm^{-2} without the voltage drop. Notably, the F-PCEE shows superior Li reversibility over 1500 h at −10 °C and 1.0 mA cm^{-2}. We attribute the high cycling performance of symmetric cells to the robust mechanical properties and high ionic conductivity of F-PCEE at a low temperature.

To highlight the potential of F-PCEE in the LMBs operating at low temperatures, we evaluated the electrochemical performances of LMBs at −10 °C configured with a 40-µm-thick Li anode, F-PCEE, and an NCM811 cathode with an active mass loading of 2.0 mg cm^{-2} at the upper cut-off voltage of 4.5 V. Before testing the cycling performance in full cells, we confirmed the high oxidation stability of F-PCEE at 4.5 V and −10 °C by conducting LSV tests at low temperatures (Figure S16, Supporting Information). As shown in **Figure 4a**, Li||F-PCEE||NCM811 cell at −10 °C delivers discharge capacities of 187, 169, 123, 83.5, and 59.7 mAh g^{-1} at 0.033, 0.05, 0.1, 0.15, and 0.2 C, respectively, and recovered to the capacity of 116 mAh g^{-1} when the current density is returned to 0.1 C. The galvanostatic charge/discharge profiles of the F-PCEE-based LMBs at various C-rates remain stable as shown in Figure 4b. We further performed the temperature-dependent charge/discharge test at 0.05 C from −20 °C to 25 °C (Figure 4c). The full cell delivers high discharge capacities of 166 and 149 mAh g^{-1} at −10 and −15 °C, respectively, corresponding to 74.4% and 66.4% of capacity utilization compared to the capacity at 25 °C, demonstrating the superior performance of F-PCEE for operating solid-state LMBs at low temperatures. When the temperature further decreases to −20 °C, the F-PCEE LMB

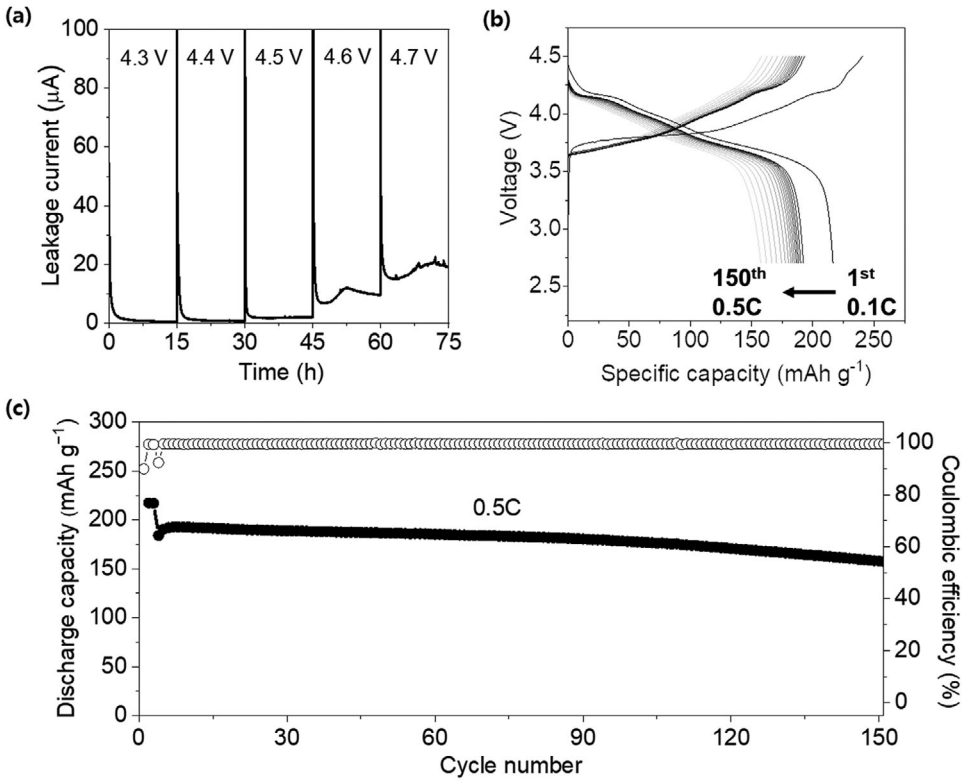

Figure 3. a) Electrochemical floating experiment with Li||F-PCEE||NCM811 at the voltage range of 4.3–4.7 V with an increment of 0.1 V. b) Voltage profiles during the cycling performance test of Li||F-PCEE||NCM811 full cell in the voltage range of 2.7–4.5 V. c) Cycling performance of full cell at 0.5 C. The cell was precycled at 0.2 C for three cycles. All tests were conducted at 25 °C. 1 C = 200 mAh g^{-1}.

exhibits a discharge capacity of 94.8 mAh g^{-1}, corresponding to 42.5% capacity utilization compared to the capacity at 25 °C.

Next, the cycling stability test of the Li||F-PCEE||NCM811 full cell was conducted at −10 °C. Here, we compare the cycling performance of the full cells using BA-PCEE to demonstrate the importance of electrolyte properties on the battery cycling performance (Figure 4d). The F-PCEE full cell showed a high capacity retention of 85.3% with an average CE of 99.2% after 150 cycles at 0.1 C. The increase in the discharge capacity during the initial 30 cycles could be attributed to the activation of the active materials.[60,61] In contrast, the full cell using BA-PCEE at −10 °C exhibited fast capacity decay with lower initial capacity at 0.1 C compared to the F-PCEE. The replicated cell performances with F-PCEE and BA-PCEE are presented in Figure S17 (Supporting Information). We attribute the poor electrochemical performance of BA-PCEE to the low σ of 0.016 mS cm^{-1} and poor U_r of 0.86 kJ m^{-3} at −10 °C (Figures 2c,d). Specifically, BA-PCEE exhibiting a discharge capacity of ≈160 mAh g^{-1} at 0.033 C experienced a significant capacity drop to 70 mAh g^{-1} at 0.1 C. Furthermore, at −10 °C, the poor mechanical resilience of BA-PCEE is insufficient to accommodate the large volume change of the Li metal and to suppress the Li dendrite growth during cycling. Electrochemical impedance spectroscopy (EIS) measurements revealed that the F-PCEE showed significantly lower ohmic (R_b), SEI layer (R_{SEI}), and charge transfer (R_{CT}) resistances than those of BA-PCEE after 150 cycles at −10 °C (Figure 4e and Figure S18, Supporting Information). These lower resistances indicate that F-PCEE forms highly conductive and kinetically favorable interphases, facilitating superior electrochemical performance of LMBs at low temperatures. Benefiting from these features of F-PCEE, the Li||F-PCEE||$LiFePO_4$ (LFP) full cell exhibited a high discharge capacity of ≈109 mAh g^{-1} and great cycling performance at −10 °C as shown in Figure S19 (Supporting Information). Thus, the F-PCEE full cell demonstrated one of the highest cycling performances among SPE-based LMBs operating at a low temperature (Table S1, Supporting Information).[23,24,62–64]

The 150-cycled Li anodes and NCM811 cathodes were further investigated to gain a deeper insight into the role of F-PCEE in enabling the superior cycling performance of LMBs at −10 °C. The surface morphologies and chemistries of the electrodes were characterized by electron microscopy and X-ray photoelectron spectroscopy (XPS), respectively. The scanning electron microscopy (SEM) image of the cycled Li metal showed a uniform and smooth surface after cycling at 25 °C and −10 °C without dendritic Li (**Figures** 5a,b). The grain size of the Li metal was slightly smaller when cycling at −10 °C than at 25 °C, possibly due to the reduced ionic conductivity and reaction kinetics at low temperatures.[7] Notably, the densely deposited Li metal morphologies of F-PCEE without dendritic Li are consistent with its cycling performance in full cells at both 25 °C and −10 °C (Figure 3c and Figure 4d). In contrast, at −10 °C, the cycled Li metal using BA-PCEE exhibited porous morphologies with mossy Li (Figure S20a, Supporting Information), which correspond to the aggravated cycling performance of BA-PCEE having

poor ionic conductivity and inferior mechanical resilience at low temperatures.

For the SEI components, the F-rich SEI layers play a crucial role in improving the cycling stability and CE of the LMBs by suppressing dendrite growth.[65–71] In particular, the LiF species with their high interfacial energy and shear modulus (58 GPa) stand out as a favorable SEI component among various inorganic components for ensuring high interfacial stability, especially in the operation of LMBs at a low temperature.[19,32,34] The high interfacial energy of LiF induces the dispersion of localized Li^+ ions and uniform deposition of Li, while the high shear modulus of LiF effectively suppresses Li dendrite growth.[72] Also, the robust and stable LiF-rich SEI layer can effectively prevent the SEI from cracking, inhibiting the continuous consumption of electrolytes and Li metal.[70,73] Nevertheless, operating LMBs at lower temperatures generally results in decreased LiF content while increasing unfavorable organic species such as RCOOLi.[31,33]

To demonstrate the importance of F-PCEE in the formation of LiF-rich SEI, we investigated the chemical composition of SEI on the 150-cycled Li metal of F-PCEE at 25 °C and −10 °C. First, the Li 1s spectra of F-PCEE show that the SEI layers contained larger amounts of inorganic species than organic species after full cell cycling at 25 °C and −10 °C (Figures 5c,d). In particular, the LiF-rich SEI layer was maintained when operating at −10 °C as confirmed by the LiF peak at 685.2 eV in the F 1s spectra, indicating the ability to form LiF-rich SEI at low temperatures.[32,34] In contrast, the Li 1s spectra of BA-PCEE after 150 cycling at −10 °C reveal a greater amount of organic components (Li-N-C, RCOOLi) compared to inorganic species (LiF, Li_2O, LiBO, Li_2CO_3) within the SEI (Figure S20b, Supporting Information). The O 1s spectra further confirm the inorganic-rich SEI layers of F-PCEE as compared to the organic-rich SEI of BA-PCEE after cycling at −10 °C (Figure S21, Supporting Information). The organic-rich SEI can lead to nonuniform Li stripping/plating and decomposition of electrolytes over cycling, explaining the inferior low-temperature performances of the BA-PCEE compared to F-PCEE.[60–63] Thus, the F-rich chemistry of F-PCEE combined with its robust mechanical properties effectively mitigated the Li dendrite growth at −10 °C through the formation of LiF-rich SEI layers.

TEM was utilized to examine the cathode-electrolyte interphase (CEI) in F-PCEE after cycling. TEM images revealed uniform and thin CEI layers with thicknesses of 3–4 and 7–8 nm for 150-cycled NCM811 at 25 °C and −10 °C, respectively (Figures 5e,f). These uniform and thin CEI layers are beneficial for Li^+ transport across the interphase. For the chemical component of the CEI layers, the relative peak intensity of C−O to C−C peak was slightly larger for cycled cathode at −10 °C (0.51) as compared to the 25 °C (0.42), which can be attributed to slower kinetics when cycling at −10 °C (Figures 5g,h).[33] The F 1s spectra indicate that the LiF-rich CEI was maintained after cycling at −10 °C as observed by the LiF peak at 685.2 eV. Specifically, cycled NCM811 at −10 °C contained 54, 28, 15, and 3% of LiF, BF, CF, and CF_2 compounds (Figure S22, Supporting Information). The stabilization of the Ni-rich cathode is critical for achieving a prolonged cycle lifetime at 4.5 V because side reactions of the cathode, including transition metal dissolution and uneven CEI layer thickening, are detrimental to the cycling lifetime of the LMBs. In particular, inorganic CEI components (e.g., LiF) can minimize the parasitic side reactions by forming a robust passivation layer on the cathode surface.[32,74–77] Thus, we further demonstrate that

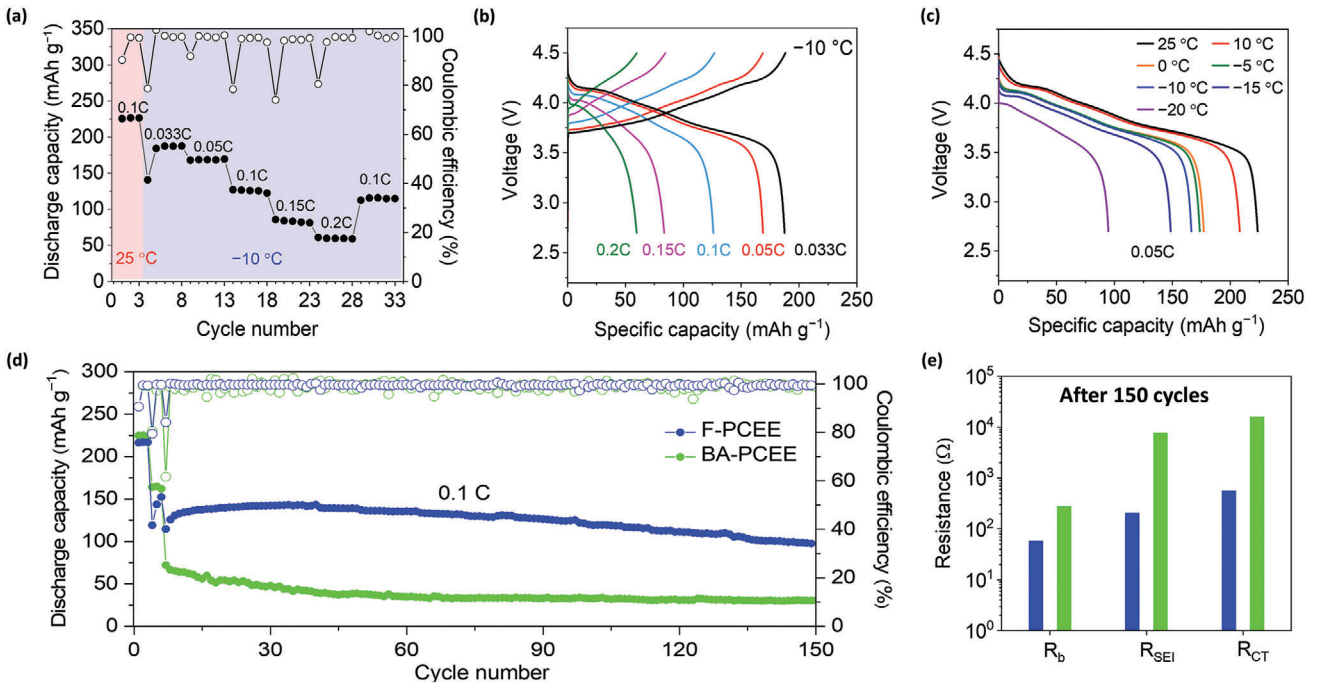

Figure 4. a) Rate performance of Li||F-PCEE||NCM811 full cell at −10 °C and b) corresponding voltage profiles. c) Temperature-dependent galvanostatic discharge profiles of the Li||F-PCEE||NCM811 full cell at 0.05 C. d) Cycling performance of the Li||F-PCEE||NCM811 and Li||BA-PCEE||NCM811 full cells at −10 °C and 0.1 C in the voltage range of 2.7–4.5 V. The first three formation cycles were conducted at 25 °C and 0.1 C. For the cycling at −10 °C, additional three formation cycles were conducted at 0.033 C. e) The R_b, R_{SEI}, and R_{CT} of F-PCEE and BA-PCEE of full cells after 150 cycles at −10 °C.

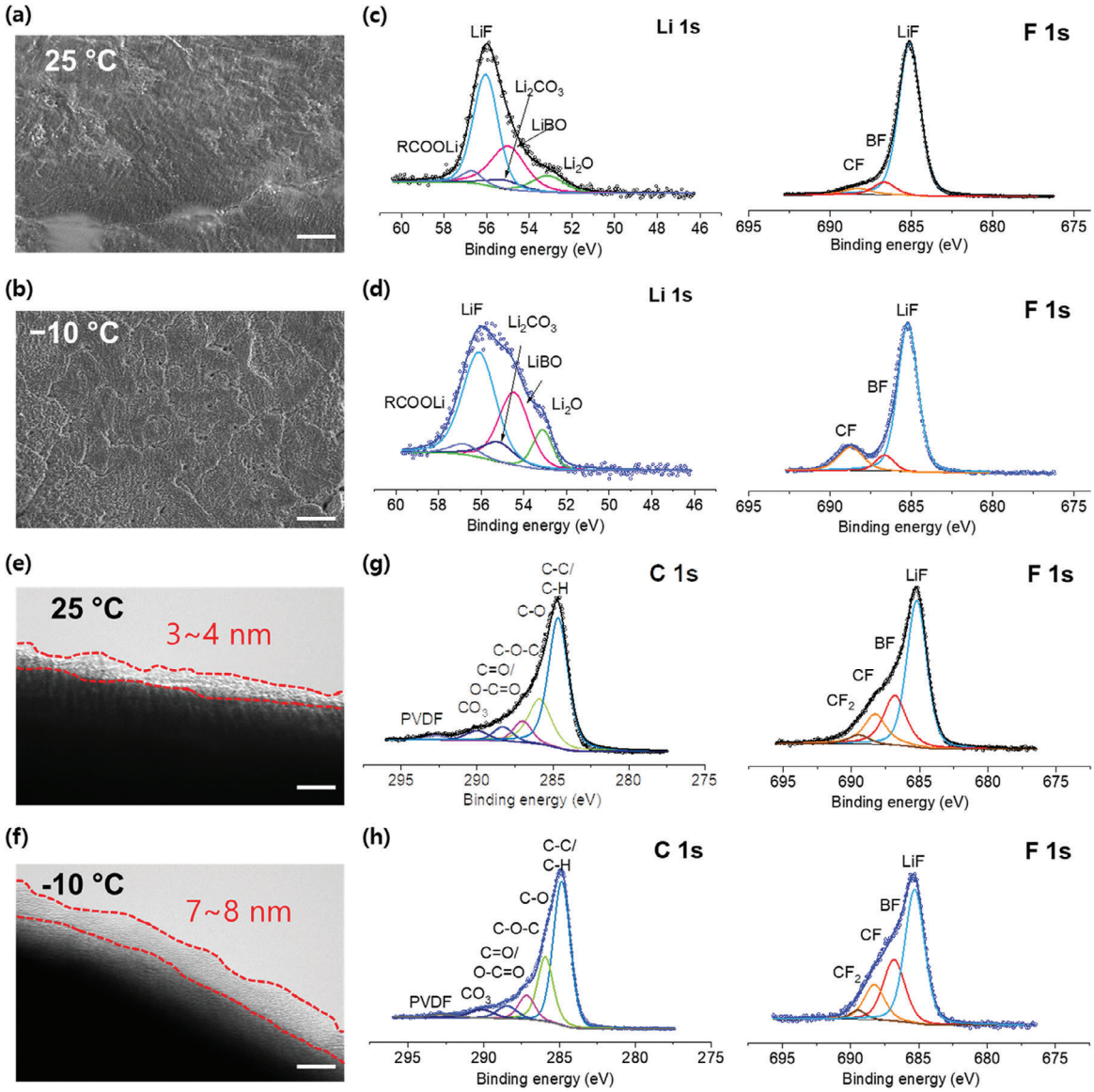

Figure 5. Characterization of cycled Li metal anode and NCM811 cathode after 150 cycles of Li||F-PCEE||NCM811 full cell at 25 and −10 °C. Top-view SEM image of Li-metal anode after cycling at a) 25 °C and b) −10 °C. The scale bars are 10 µm. Corresponding Li 1s and F 1s XPS spectra of Li metal anode after cycling at c) 25 °C and d) −10 °C. TEM image of NCM811 cathode after cycling at e) 25 °C and f) −10 °C. The scale bars are 10 nm. Corresponding C 1s and F 1s XPS spectra of NCM811 cathode after cycling at g) 25 °C and h) −10 °C.

the F-PCEE facilitates the formation of robust LiF-rich CEI layers, contributing to the stabilization of the NCM811 cathode in LMBs.

To elucidate the role of mechanical resilience on electrochemical performance, we illustrate the mechanisms of full cells using either F-PCEE or BA-PCEE when cycling at low temperatures (**Scheme 2**). When charging at −10 °C, the Li metal anode in the full cell using F-PCEE exhibits more favorable Li deposition compared to that in the full cell using BA-PCEE, due to the superior ionic conductivity of F-PCEE. Furthermore, the mechanical resilience of elastomeric electrolytes is crucial for maintaining interfacial contact between the electrolytes and Li metal electrodes during cell cycling.[47] Specifically, the F-PCEE with high mechanical resilience can accommodate the large volume change and suppress the nucleation of Li dendrite growth, thereby maintaining its stable contact with Li metal anode upon discharging (Scheme 2a). In contrast, the permanent deformation of BA-PCEE during charging causes a loss of contact between the electrolyte and electrode after discharging, due to its poor mechanical resilience (Scheme 2b). Therefore, the lack of uniform Li^+ flux and high interfacial resistance in the BA-PCEE can exacerbate the electrochemical performance of the full cell during repeated charge and discharge cycles at low temperatures.

3. Conclusions

We developed a fluorinated elastomeric electrolyte for achieving solid-state LMBs operating at low temperatures and high voltages. The F-PCEE was fabricated via polymerization-induced

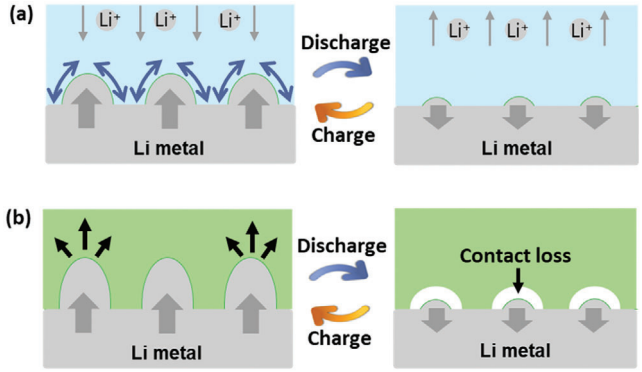

Scheme 2. Schematic illustrations of the proposed mechanism for the different cycling performances of a full cell using either a) F-PCEE or b) BA-PCEE at low temperatures.

phase separation between the poly(HFBA) and SN phases. The selective localization of Li^+ through the strong phase separation of two phases resulted in robust mechanical properties (e.g., a mechanical strain of ≈300% and U_r = 52.7 kJ m^{-3}) and a high σ of 0.23 mS cm^{-1} at −10 °C. These combined features contributed to the superior cycling performance in the Li||F-PCEE||Li symmetric cell at −10 °C and 1.0 mA cm^{-2} with a cycling lifetime exceeding 1500 h. In the Li||F-PCEE||NCM811 full cell operating at −10 °C and a high cut-off voltage of 4.5 V, an outstanding cycling performance of ≈85.3% capacity retention after 150 cycles was attributed to the densely deposited Li, LiF-rich SEI layer, and robust CEI layer. The role of F-PCEE in operating LMBs at low temperatures has been investigated by comparing its temperature-dependent mechanical properties and electrochemical performances with those of the BA-PCEE. Thus, this work highlights the design principle of elastomeric electrolytes for developing high-performance solid-state LMBs for applications in low-temperature environments.

4. Experimental Section

Polymer Electrolyte Preparation: F-PCEE and BA-PCEE were fabricated in an argon gas-filled glove box (<0.1 ppm of O_2 and H_2O). Both HFBA and BA were degassed via argon gas bubbling for 30 min before use. SN was used after repeated freeze-pump-thaw cycles. The F-PCEE precursor solution was prepared by mixing HFBA-based and SN-based solutions with varying f_{SN}, which represents the (volume of SN)/(volume of SN + volume of HFBA) within the mixed solution. HFBA-based solutions were prepared by dissolving 4 mol% PEGDA (M_n = 575 g mol^{-1}) in HFBA monomer. The SN-based solutions were prepared by dissolving LiTFSI and LiDFOB. The salt concentration within the F-PCEE precursor solution is fixed to 0.8 M LiTFSI and 0.2 M LiDFOB. A 4 vol% of fluoroethylene carbonate (FEC) was added to prevent side reactions of SN with Li metal. Subsequently, 0.5 mol% AIBN was added to the mixture and stirred for 3 min to make the homogeneous F-PCEE precursor solution. The F-PCEE precursor solution was polymerized at 70 °C for 2 h to obtain F-PCEE. In a similar procedure to F-PCEE, the BA-PCEE was synthesized from the precursor solution containing the same volume ratio of BA and SN, 1 mol% PEGDA, 0.8 M LiTFSI, 0.2 M LiDFOB, 4 vol% FEC, and 0.5 mol% AIBN.

Material Characterization: ^{7}Li solid-state NMR spectra were obtained from a 500 MHz Avance III HD Bruker Solid-state NMR. Due to the moisture sensitivity of ^{7}Li solid-state NMR measurements, prepared F-PCEE and BA-PCEE samples were sealed inside a poly(chlorotrifluoroethylene) rotor within a glove box. The obtained NMR spectra were referenced to a 1 M LiCl aqueous solution at 0 ppm. TGA (TA instruments Q500) was measured from 45 °C to 700 °C at a heating rate of 10 °C min^{-1} under a nitrogen atmosphere. DSC graphs were obtained using a TA instrument Q200 under a nitrogen atmosphere at a cooling and a heating rate of 10 °C min^{-1}. The FT-IR was carried out in the attenuated total reflection mode using a Brucker ALPHA-P spectrometer. Mechanical tensile test was performed using UTM (Shimadzu AG-X Plus 50 kN) with a 100 N load cell at 100 mm min^{-1}. Bulk samples were prepared in a Teflon mold (ASTM D 638 type 4). Cryo-TEM specimens were prepared as follows. F-PCEE was rapidly quenched in liquid nitrogen for 10 s. A Leica EM FC7 ultramicrotome containing a cryo chamber, equipped with a glass knife and set to a cutting rate of 0.3 mm s^{-1}, was used to section the vitrified F-PCEE. The sample face for the sample preparation was approximately 200 × 200 µm. The ultrathin film, about 50 nm thick and maintained at temperatures between −80 °C to −75 °C, was transferred onto a 200 mesh carbon-coated copper grid (Electron Microscopy Sciences). Cross-sectional images were acquired using a JEOL JEM-1400 (JEOL Ltd., Tokyo, Japan) operating at 120 kV equipped with a Gatan 914 cryo-holder (Gatan Inc.). The TEM images were recorded with a 1 s exposure time utilizing a Veleta charge-coupled device camera (EMSIS GmbH). Data were analyzed with the RADIUS imaging software (Olympus Soft Imaging Solutions). For the adhesion test, F-PCEE was in situ polymerized between the NCM811 cathodes, and the adhesion energy was measured by using UTM.

The chemical compositions of SEI and CEI formed on the Li metal anode and NCM811 cathode were characterized by XPS measurements (Thermal Scientific Nexsa G2). After full cell cycling, the cells were disassembled in an argon-filled glove box. Then Li metal and NCM811 cathodes were transferred to XPS using a vacuum transfer holder to prevent any side reaction from ambient oxygen and moisture. The morphology of the cycled-Li metal was characterized by SEM measurements (Hitachi SU8230). The morphology of CEI after cell cycling was observed by TEM measurements (Tecnai G2 F30 S-Twin). TEM samples were collected from the disassembled NCM811 electrodes and loaded on a lacey carbon-coated TEM grid.

Positive Electrode Preparation: NCM811 and LFP cathodes were prepared by a slurry coating method. The slurry was made by mixing 80 wt% active material, 10 wt% Super P carbon as a conductive carbon, and 10 wt% poly(vinylidene fluoride) as a binder in an *N*-methyl-2-pyrrolidone for 18 h. The slurry was coated onto a carbon-coated Al foil and then dried at 90 °C for 30 min. The mass loading of active materials was ≈2.0 mg cm^{-2}.

Electrochemical Measurement: The electrochemical performance tests were carried out using 2032-type coin cells in an argon-filled glovebox (<0.1 ppm of O_2 and H_2O). Depending on the characterization techniques, appropriate electrodes were selected from stainless steel (SS), Li foil, and NCM811 or LFP electrodes. For in situ polymerization, the homogeneous precursor solution was injected into a 14µm-thick poly(propylene) or 260µm-thick glass fiber to prevent a short circuit in a coin cell. The crimped coin cell was placed in an oven at 70 °C for 2 h. The ionic conductivities were measured with SS||SS symmetric cells in an environmental chamber (Jeio Tech TC3-KE-025) using EIS measurements (Bio-Logic SP-200). To investigate the electrochemical stability between Li and F-PCEE, Li||F-PCEE||Li symmetric coin cells were assembled without a separator.[37] LSV was carried out using Li||SS asymmetric cells from 1.5 to 7 V versus Li/Li^+ at a scan rate of 1 mV s^{-1}.

For the fabrication of full cells with NCM811 or LFP cathodes, the precursor solution was infiltrated into the electrodes to improve the interfacial contact between the electrolyte and electrode. The electrochemical floating test was carried out in the fully charged states of Li||NCM811 full cells from 4.3 to 4.7 V versus Li/Li^+ with voltage holding for 15 h. The galvanostatic charge/discharge tests were performed in the voltage range of 2.7–4.5 V for 40-µm-thick Li||NMC811 and 2.5 – 4.0 V for 40-µm-thick Li||LFP to evaluate the cycling performance and rate capabilities with three formation cycles at 0.1 C and 25 °C before main cycling. For the cycling performance at −10 °C, three times of additional formation cycles were performed at a current rate of 0.033 C. All cell performance tests were carried

out in an environmental chamber to maintain a desired temperature. To investigate the variation of resistance factors in full cells upon cycling, EIS was measured from 5 MHz to 2 mHz.

Supporting Information

Supporting Information is available from the Wiley Online Library or from the author.

Acknowledgements

J.P. and H.S. contributed equally to this work. This work was supported by Samsung Research Funding & Incubation Center of Samsung Electronics under Project. Number SRFC-MA2201-04.

Conflict of Interest

The authors declare no conflict of interest

Data Availability Statement

The data that support the findings of this study are available from the corresponding author upon reasonable request.

Keywords

fluorine chemistry, lithium metal battery, low temperature, polymer electrolyte, solid state electrolyte

Received: March 1, 2024
Revised: April 28, 2024
Published online:

[1] J. M. Tarascon, M. Armand, *Nature* **2001**, *414*, 359.
[2] W. Xu, J. Wang, F. Ding, X. Chen, E. Nasybulin, Y. Zhang, J. G. Zhang, *Energy Environ. Sci.* **2014**, *7*, 513.
[3] D. Lin, Y. Liu, Y. Cui, *Nat. Nanotechnol.* **2017**, *12*, 194.
[4] J. Hou, M. Yang, D. Wang, J. Zhang, *Adv. Energy Mater.* **2020**, *10*, 1904152.
[5] D. Luo, M. Li, Y. Zheng, Q. Ma, R. Gao, Z. Zhang, H. Dou, G. Wen, L. Shui, A. Yu, X. Wang, Z. Chen, *Adv. Sci.* **2021**, *8*, 2101051.
[6] J. Wu, Y. Wu, L. Wang, H. Ye, J. Lu, Y. Li, *Adv. Mater.* **2023**, *36*, 2308193.
[7] A. Hu, F. Li, W. Chen, T. Lei, Y. Li, Y. Fan, M. He, F. Wang, M. Zhou, Y. Hu, Y. Yan, B. Chen, J. Zhu, J. Long, X. Wang, J. Xiong, *Adv. Energy Mater.* **2022**, *12*, 2202432.
[8] M. T. F. Rodrigues, G. Babu, H. Gullapalli, K. Kalaga, F. N. Sayed, K. Kato, J. Joyner, P. M. Ajayan, *Nat. Energy* **2017**, *2*, 17108.
[9] N. Zhang, T. Deng, S. Zhang, C. Wang, L. Chen, C. Wang, X. Fan, *Adv. Mater.* **2022**, *34*, 2107899.
[10] X. B. Cheng, R. Zhang, C. Z. Zhao, Q. Zhang, *Chem. Rev.* **2017**, *117*, 10403.
[11] S. Xia, X. Wu, Z. Zhang, Y. Cui, W. Liu, *Chem* **2019**, *5*, 753.
[12] Y. G. Lee, S. Fujiki, C. Jung, N. Suzuki, N. Yashiro, R. Omoda, D. S. Ko, T. Shiratsuchi, T. Sugimoto, S. Ryu, J. H. Ku, T. Watanabe, Y. Park, Y. Aihara, D. Im, I. T. Han, *Nat. Energy* **2020**, *5*, 299.
[13] R. Chen, Q. Li, X. Yu, L. Chen, H. Li, *Chem. Rev.* **2020**, *120*, 6820.
[14] H. Wang, L. Sheng, G. Yasin, L. Wang, H. Xu, X. He, *Energy Storage Mater.* **2020**, *33*, 188.
[15] J. Zhu, Z. Zhang, S. Zhao, A. S. Westover, I. Belharouak, P. F. Cao, *Adv. Energy Mater.* **2021**, *11*, 2003836.
[16] P. Lennartz, B. A. Paren, A. Herzog-Arbeitman, X. C. Chen, J. A. Johnson, M. Winter, Y. Shao-Horn, G. Brunklaus, *Joule* **2023**, *7*, 1471.
[17] Q. Zhao, X. Liu, S. Stalin, K. Khan, L. A. Archer, *Nat. Energy* **2019**, *4*, 365.
[18] J. Mindemark, M. J. Lacey, T. Bowden, D. Brandell, *Prog. Polym. Sci.* **2018**, *81*, 114.
[19] Z. Yu, Y. Cui, Z. Bao, *Cell Rep. Phys. Sci.* **2020**, *1*, 100119.
[20] Y. Zhou, F. Zhang, P. He, Y. Zhang, Y. Sun, J. Xu, J. Hu, H. Zhang, X. Wu, *J. Energy Chem.* **2020**, *46*, 87.
[21] J. Yu, X. Lin, J. Liu, J. T. T. Yu, M. J. Robson, G. Zhou, H. M. Law, H. Wang, B. Z. Tang, F. Ciucci, *Adv. Energy Mater.* **2022**, *12*, 2102932.
[22] H. He, Y. Wang, M. Li, J. Qiu, Y. Wen, J. Chen, *Chem. Eng. J.* **2023**, *467*, 143311.
[23] X. Zhang, C. Fu, S. Cheng, C. Zhang, L. Zhang, M. Jiang, J. Wang, Y. Ma, P. Zuo, C. Du, Y. Gao, G. Yin, H. Huo, *Energy Storage Mater.* **2023**, *56*, 121.
[24] S. Xu, Z. Sun, C. Sun, F. Li, K. Chen, Z. Zhang, G. Hou, H. M. Cheng, F. Li, *Adv. Funct. Mater.* **2020**, *30*, 2007172.
[25] J. Li, Y. Cai, Y. Cui, H. Wu, H. Da, Y. Yang, H. Zhang, S. Zhang, *Nano Energy* **2022**, *95*, 107027.
[26] Y. Wang, Z. Chen, Y. Wu, Y. Li, Z. Yue, M. Chen, *ACS Appl. Mater. Interfaces* **2023**, *15*, 21526.
[27] S. Liu, W. Liu, D. Ba, Y. Zhao, Y. Ye, Y. Li, J. Liu, *Adv. Mater.* **2023**, *35*, 2110423.
[28] X. Kong, P. E. Rudnicki, S. Choudhury, Z. Bao, J. Qin, *Adv. Funct. Mater.* **2020**, *30*, 1910138.
[29] B. Zhu, Y. Jin, X. Hu, Q. Zheng, S. Zhang, Q. Wang, J. Zhu, *Adv. Mater.* **2017**, *29*, 1603755.
[30] G. M. Stone, S. A. Mullin, A. A. Teran, D. T. Hallinan, A. M. Minor, A. Hexemer, N. P. Balsara, *J. Electrochem. Soc.* **2012**, *159*, A222.
[31] J. Holoubek, M. Yu, S. Yu, M. Li, Z. Wu, D. Xia, P. Bhaladhare, M. S. Gonzalez, T. A. Pascal, P. Liu, Z. Chen, *ACS Energy Lett* **2020**, *5*, 1438.
[32] Z. Li, R. Yu, S. Weng, Q. Zhang, X. Wang, X. Guo, *Nat. Commun.* **2023**, *14*, 482.
[33] S. Weng, X. Zhang, G. Yang, S. Zhang, B. Ma, Q. Liu, Y. Liu, C. Peng, H. Chen, H. Yu, X. Fan, T. Cheng, L. Chen, Y. Li, Z. Wang, X. Wang, *Nat. Commun.* **2023**, *14*, 4474.
[34] Y. Gao, T. Rojas, K. Wang, S. Liu, D. Wang, T. Chen, H. Wang, A. T. Ngo, D. Wang, *Nat. Energy* **2020**, *5*, 534.
[35] M. W. Schulze, L. D. McIntosh, M. A. Hillmyer, T. P. Lodge, *Nano Lett.* **2014**, *14*, 122.
[36] T. Oh, S. Cho, C. Yoo, W. Yeo, J. Oh, M. Seo, *Prog. Polym. Sci.* **2023**, *145*, 101738.
[37] M. J. Lee, J. Han, K. Lee, Y. J. Lee, B. G. Kim, K. N. Jung, B. J. Kim, S. W. Lee, *Nature* **2022**, *601*, 217.
[38] J. Han, M. J. Lee, K. Lee, Y. J. Lee, S. H. Kwon, J. H. Min, E. Lee, W. Lee, S. W. Lee, B. J. Kim, *Adv. Mater.* **2023**, *35*, 2205194.
[39] S. H. Kwon, M. J. Lee, J. Han, J. H. Min, S. Kim, S. Y. Kim, J. Park, E. Lee, S. W. Lee, B. Kim, *J. Mater. Chem. A* **2024**, *12*, 3460.
[40] K. Park, S. Yu, C. Lee, H. Lee, *J. Power Sources* **2015**, *296*, 197.
[41] A. Gabryelczyk, S. Ivanov, A. Bund, G. Lota, *J. Energy Storage* **2021**, *43*, 103226.
[42] L. Chen, W. A. Phillip, E. L. Cussler, M. A. Hillmyer, *J. Am. Chem. Soc.* **2007**, *129*, 13786.
[43] M. Putz, M. Dix, M. Neubert, G. Schmidt, R. Wertheim, *Proc. CIRP* **2016**, *40*, 631.
[44] P. Maurya, G. S. Vijay, C. Raghavendra Kamath, B. Shivamurthy, *Mach. Sci. Technol.* **2021**, *25*, 477.
[45] P. Maurya, G. S. Vijay, R. C. Kamath, *Mater Today Proc.* **2023**, https://doi.org/10.1016/j.matpr.2023.03.451.
[46] Y. Shi, N. Yang, J. Niu, S. Yang, F. Wang, *Adv. Sci.* **2022**, *9*, 2200553.
[47] J. Lopez, Y. Sun, D. G. Mackanic, M. Lee, A. M. Foudeh, M. S. Song, Y. Cui, Z. Bao, *Adv. Mater.* **2018**, *30*, 1804142.

[48] Q. Ma, S. Liao, Y. Ma, Y. Chu, Y. Wang, *Adv. Mater.* **2021**, *33*, 2102096.
[49] J. Cannarella, X. Liu, C. Z. Leng, P. D. Sinko, G. Y. Gor, C. B. Arnold, *J. Electrochem. Soc.* **2014**, *161*, F3117.
[50] E. Quartarone, P. Mustarelli, *Chem. Soc. Rev.* **2011**, *40*, 2525.
[51] N. S. Schauser, D. J. Grzetic, T. Tabassum, G. A. Kliegle, M. L. Le, E. M. Susca, S. Antoine, T. J. Keller, K. T. Delaney, S. Han, R. Seshadri, G. H. Fredrickson, R. A. Segalman, *J. Am. Chem. Soc.* **2020**, *142*, 7055.
[52] J. Imbrogno, K. Maruyama, F. Rivers, J. R. Baltzegar, Z. Zhang, P. W. Meyer, V. Ganesan, S. Aoshima, N. A. Lynd, *ACS Macro Lett.* **2021**, *10*, 1002.
[53] N. A. Stolwijk, C. Heddier, M. Reschke, M. Wiencierz, J. Bokeloh, G. Wilde, *Macromolecules* **2013**, *46*, 8580.
[54] A. J. Butzelaar, P. Röring, T. P. Mach, M. Hoffmann, F. Jeschull, M. Wilhelm, M. Winter, G. Brunklaus, P. Théato, *ACS Appl. Mater. Interfaces* **2021**, *13*, 39257.
[55] S. Lascaud, M. Perrier, A. Vallée, S. Besner, J. Prud'homme, M. Armand, *Macromolecules* **1994**, *27*, 7469.
[56] V. Bocharova, A. P. Sokolov, *Macromolecules* **2020**, *53*, 4141.
[57] B. Xu, Z. Liu, J. Li, X. Huang, B. Qie, T. Gong, L. Tan, X. Yang, D. Paley, M. Dontigny, K. Zaghib, X. Liao, Q. Cheng, H. Zhai, X. Chen, L. Q. Chen, C. W. Nan, Y. H. Lin, Y. Yang, *Nano Energy* **2020**, *67*, 104242.
[58] A. Hu, W. Chen, F. Li, M. He, D. Chen, Y. Li, J. Zhu, Y. Yan, J. Long, Y. Hu, T. Lei, B. Li, X. Wang, J. Xiong, *Adv. Mater.* **2023**, *35*, 2304762.
[59] V. Barreau, D. Yu, R. Hensel, E. Arzt, *J. Mech. Behav. Biomed. Mater.* **2017**, *76*, 110.
[60] S. Y. Luchkin, M. A. Kirsanova, D. A. Aksyonov, S. A. Lipovskikh, V. A. Nikitina, A. M. Abakumov, K. J. Stevenson, *ACS Appl. Energy Mater.* **2022**, *5*, 7758.
[61] D. Ye, G. Zeng, K. Nogita, K. Ozawa, M. Hankel, D. J. Searles, L. Wang, *Adv. Funct. Mater.* **2015**, *25*, 7488.
[62] Z. Lin, X. Guo, Z. Wang, B. Wang, S. He, L. A. O'Dell, J. Huang, H. Li, H. Yu, L. Chen, *Nano Energy* **2020**, *73*, 104786.
[63] H. Wu, B. Tang, X. Du, J. Zhang, X. Yu, Y. Wang, J. Ma, Q. Zhou, J. Zhao, S. Dong, G. Xu, J. Zhang, H. Xu, G. Cui, L. Chen, *Adv. Sci.* **2020**, *7*, 2003370.
[64] A. Wang, S. Geng, Z. Zhao, Z. Hu, J. Luo, *Adv. Funct. Mater.* **2022**, *32*, 2201861.
[65] Y. Lu, Z. Tu, L. A. Archer, *Nat. Mater.* **2014**, *13*, 961.
[66] X. Fan, L. Chen, O. Borodin, X. Ji, J. Chen, S. Hou, T. Deng, J. Zheng, C. Yang, S. C. Liou, K. Amine, K. Xu, C. Wang, *Nat. Nanotechnol.* **2018**, *13*, 715.
[67] X. Fan, X. Ji, L. Chen, J. Chen, T. Deng, F. Han, J. Yue, N. Piao, R. Wang, X. Zhou, X. Xiao, L. Chen, C. Wang, *Nat. Energy* **2019**, *4*, 882.
[68] X. Wang, J. Lu, Y. Wu, W. Zheng, H. Zhang, T. Bai, H. Liu, D. Li, L. Ci, *Adv. Mater.* **2024**, *36*, 2311256.
[69] N. Mubarak, F. Rehman, M. Ihsan-Ul-Haq, M. Xu, Y. Li, Y. Zhao, Z. Luo, B. Huang, J. K. Kim, *Adv. Energy Mater.* **2022**, *12*, 2103904.
[70] K. Huang, S. Song, Z. Xue, X. Niu, X. Peng, Y. Xiang, *Energy Storage Mater.* **2023**, *55*, 301.
[71] M. Xu, Y. Li, M. Ihsan-Ul-Haq, N. Mubarak, Z. Liu, J. Wu, Z. Luo, J. K. Kim, *Energy Storage Mater.* **2022**, *44*, 477.
[72] X. Jian Hu, Y. Ping Zheng, Z. Wei Li, C. Xia, D. H. C. Chua, X. Hu, T. Liu, X. Bin Liu, Z. Ping Wu, B. Yu Xia, *Angew. Chem. Int. Ed.* **2024**, *63*, 202319600.
[73] P. Liu, H. Su, Y. Liu, Y. Zhong, C. Xian, Y. Zhang, X. Wang, X. Xia, J. Tu, *Small Struct.* **2022**, *3*, 2200010.
[74] X. Fan, L. Chen, X. Ji, T. Deng, S. Hou, J. Chen, J. Zheng, F. Wang, J. Jiang, K. Xu, C. Wang, *Chem* **2018**, *4*, 174.
[75] X. Cao, X. Ren, L. Zou, M. H. Engelhard, W. Huang, H. Wang, B. E. Matthews, H. Lee, C. Niu, B. W. Arey, Y. Cui, C. Wang, J. Xiao, J. Liu, W. Xu, J. G. Zhang, *Nat. Energy* **2019**, *4*, 796.
[76] W. Xue, Z. Shi, M. Huang, S. Feng, C. Wang, F. Wang, J. Lopez, B. Qiao, G. Xu, W. Zhang, Y. Dong, R. Gao, Y. Shao-Horn, J. A. Johnson, J. Li, *Energy Environ. Sci.* **2020**, *13*, 212.
[77] W. Xue, M. Huang, Y. Li, Y. G. Zhu, R. Gao, X. Xiao, W. Zhang, S. Li, G. Xu, Y. Yu, P. Li, J. Lopez, D. Yu, Y. Dong, W. Fan, Z. Shi, R. Xiong, C. J. Sun, I. Hwang, W. K. Lee, Y. Shao-Horn, J. A. Johnson, J. Li, *Nat. Energy* **2021**, *6*, 495.